Research paper

Effect of cross derivatives in discretization schemes in structured non-orthogonal meshes for compositional reservoir simulation

Francisco Marcondes [a], Choongyong Han [b], Kamy Sepehrnoori [c],*

[a] *Department of Metallurgical Engineering and Material Science, Federal University of Ceará, Fortaleza, Ceará, Brazil*
[b] *Center for Petroleum and Geosystems Engineering, The University of Texas at Austin, Austin, TX, USA. Now in Chevron ETC, Houston, TX, USA*
[c] *Petroleum and Geosystems Engineering Department, The University of Texas at Austin, 1 University Station C0300, Austin, TX 78712-0228, USA*

ARTICLE INFO

ABSTRACT

Corner-point meshes have been implemented in several commercial reservoir simulators due to their flexibility to deal with several important features of the hydrocarbon bearing-reservoirs, such as irregular boundaries, geologic fractures, and faults. Although this type of mesh presents an important step in discretization of the domains for reservoirs, some parts of the approximate equation in discretized formulations are neglected in most commercial simulators. The neglected terms are related to the cross derivatives and, in general, are neglected to produce the same Jacobian stencil as when Cartesian grids are employed. This work presents an investigation of the effect of cross derivatives in discretization schemes using structured non-orthogonal boundary-fitted meshes in conjunction with a compositional reservoir simulator. The main goal is to investigate the difference between the numerical results with and without the cross derivatives that arise when the Cartesian equations are written for a transformed plane. We used an in-house compositional reservoir simulator to carry out this study. The component mass balance equations for a compositional, multiphase, multi-component fluid flow are solved using a fully implicit reservoir simulator in conjunction with the finite volume method. The results of several reservoir simulation case studies that were performed to carry out this study are presented in this paper.

© 2008 Elsevier B.V. All rights reserved.

1. Introduction

Cartesian grids have been used in petroleum reservoir simulation because accumulation terms and fluxes are easily evaluated using this type of grids. On the other hand, when using Cartesian grids, the correct representation of several features of the reservoir such as faults, fractures, and irregular boundaries are not easily handled. One option for the Cartesian grids is the boundary-fitted coordinates (Sheldon and Dougherty, 1961; Hirasaki and O'Dell, 1970; Wadsley, 1980). These authors have employed orthogonal boundary-fitted coordinates in their works. Although orthogonal boundary-fitted coordinates are one improvement for Cartesian grids, this type of grid still presents some drawbacks. Possibly the most import drawback is the orthogonal restriction of surfaces in a 3D case or lines in a 2D case. To eliminate this restriction, non-orthogonal boundary-fitted coordinates must be employed (Leventhal et al., 1985; Maliska et al., 1997; Edwards, 1998a; Prévost and Edwards, 2002; Marcondes et al., 2005a,b). One problem that arises when using non-orthogonal meshes is that the Jacobian stencil changes from five and seven to nine and nineteen for 2D and 3D cases, respectively. One common approach to simplify the Jacobian stencil when using non-orthogonal boundary-

fitted coordinates is to neglect the additional terms that arise in the Jacobian matrix due to geometric transformation. This is done in most commercial simulators. An investigation of the importance of these terms in water-flooding reservoir simulations has been performed by Marcondes et al. (2005b). In that work, it was shown that the cross derivatives play an important role when the mesh is distorted. More importantly, it was also shown that when the cross derivatives are ignored, the solution does not converge as the mesh is refined.

All the previous publications that have investigated the importance of cross derivatives for evaluation of mass flow rate have carried out their investigations using water flooding or black-oil simulations (Hegre et al., 1986; Aziz 1993; Edwards, 1998b; Edwards and Rogers, 1998). To the best of our knowledge, the investigation of cross derivatives has not been done yet for a compositional reservoir simulator.

In this study, non-orthogonal boundary-fitted meshes have been included in an in-house compositional reservoir simulator called GPAS (General Purpose Adaptive Simulator). This simulator was developed at the Center for Petroleum and Geosystems Engineering for simulation of enhanced oil recovery processes (Wang et al., 1997). GPAS is a 3D, fully implicit, multiphase/multi-component, parallel reservoir simulator that can handle simulation of several enhanced oil recovery processes. In parallel mode, message passing between the processors is performed using MPI (Gropp et al., 1999). GPAS is divided into two main modules: Framework and EOScomp. Framework is responsible for input/output,

---

domain decomposition, and memory allocation, while EOScomp handles the computations for flash calculation and solution of nonlinear equations arising from discretization of the governing equations. Details of EOScomp and Framework modules can be found in Wang et al. (1997) and Parashar et al. (1997), respectively.

The main focus of this paper is to investigate the influence of cross derivatives in evaluation of mass flux rate using GPAS. In the following sections, we present the physical model, the approximate equations, the test problems, the results of simulation case studies, and the main conclusions of this investigation.

2. Physical model

Isothermal, multi-component, multiphase fluid flow in a porous medium can be described using three types of equations: the component-material balance equation, phase equilibrium equation, and equation for constraining phase saturations and component concentrations (Wang et al., 1997).

The material balance equation for the i-th component for a full symmetric permeability tensor can be written in a Cartesian system as

$$
\begin{aligned}
\frac{\partial(\phi N_i)}{\partial t} - \frac{\partial}{\partial x} &\left(\sum_{j=1}^{np} \xi_j x_{ij} \lambda_{rj} K_{xx} \frac{\partial \Phi_j}{\partial x} + \xi_j x_{ij} \lambda_{rj} K_{xy} \frac{\partial \Phi_j}{\partial y} + \xi_j x_{ij} \lambda_{rj} K_{xz} \frac{\partial \Phi_j}{\partial z} \right) \\
- \frac{\partial}{\partial y} &\left(\sum_{j=1}^{np} \xi_j x_{ij} \lambda_{rj} K_{xy} \frac{\partial \Phi_j}{\partial x} + \xi_j x_{ij} \lambda_{rj} K_{yy} \frac{\partial \Phi_j}{\partial y} + \xi_j x_{ij} \lambda_{rj} K_{yz} \frac{\partial \Phi_j}{\partial z} \right) \\
- \frac{\partial}{\partial z} &\left(\sum_{j=1}^{np} \xi_j x_{ij} \lambda_{rj} K_{xz} \frac{\partial \Phi_j}{\partial x} + \xi_j x_{ij} \lambda_{rj} K_{yz} \frac{\partial \Phi_j}{\partial y} + \xi_j x_{ij} \lambda_{rj} K_{zz} \frac{\partial \Phi_j}{\partial z} \right) \\
&- \frac{q_i}{V_b} = 0; i = 1, 2, .., n_c + 1
\end{aligned}
\tag{1}
$$

where n_c is the number of hydrocarbon components, $n_c + 1$ denotes the water component, n_p is the number of phases present in the reservoir, ϕ is the porosity, N_i is the moles of the i-th component per unit of pore volume, ξ_j and λ_{rj} are the molar density and relative
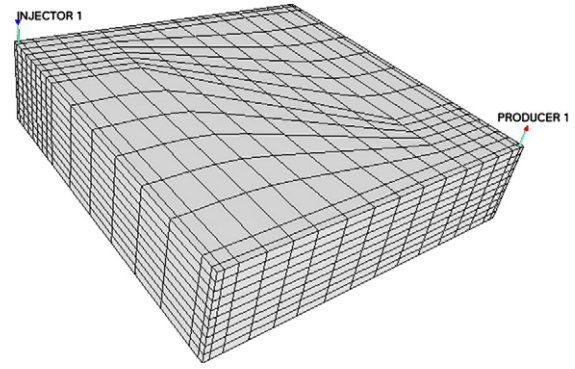

Fig. 1. (a) Physical and computational domains (b) control volume.

Fig. 2. Non-orthogonal mesh for case 1.

mobility of the j-th phase respectively, x_{ij} is the molar fraction of the i-th component in the j-th phase, K_{xx}, K_{xy}, K_{xz}, K_{yy}, K_{yz}, and K_{zz} are the entries of the absolute permeability tensor, and V_b is the bulk volume of block. Φ_j is the potential of the j-th phase and is given by

$$
\Phi_j = P_j - \gamma_j Z
\tag{2}
$$

In Eq. (2), P_j denotes the pressure of the j-th phase and Z is depth, which is positive in a downward direction.

The first partial derivative of the total Gibbs free energy with respect to the independent variables gives the equality of component fugacities among all phases,

$$
f_i = f_i^j - f_i^r = 0 \quad ; \quad i = 1, ..., n_c \quad ; \quad j = 2, ..., n_p
\tag{3}
$$

In Eq. (3), $f_i^j = \ln(x_{ij} \phi_{ij})$, where ϕ_{ij} is the fugacity coefficient of component i in the j-th phase, r denotes the reference phase. The restriction of the molar fraction is used to obtain the solution of Eq. (3),

$$
\sum_{i=1}^{n_c} x_{ij} - 1 = 0, j = 2, .., n_p \quad ; \quad \sum_{i=1}^{n_c} \frac{z_i(K_i - 1)}{1 + v(K_i - 1)} = 0
\tag{4}
$$

where z_i is the overall molar fraction of the i-th component, K_i is the equilibrium ratio for the i-th component, and ν is the mole fraction of the gas phase in the absence of water. The closure equation comes from the volume constraint, that is, the available pore volume of each cell must be filled by all phases present in the reservoir. This constraint gives rise to the following equation:

$$
V_b \sum_{i=1}^{n_c+1} (\phi N_i) \sum_{j=1}^{n_p} L_j \bar{v}_j - V_p = 0
\tag{5}
$$

where V_p is the pore volume, and $\bar{v}_j$ is the molar volume of the j-th phase. In GPAS the unknown primary variables are water pressure P_w, $N_1,...,N_{nc}$, $\ln K_1,..., \ln K_{nc.}$

3. Transformed and approximate equations

In the approach adopted in this work, the equations are transformed from the Cartesian system to a computational domain. Subsequently, the transformed equations are integrated into the regular system, as described in Maliska (2004). From the set of equations described in the previous section, the only equation that needs to be written in the computational plane is the molar mass balance equation for each component, Eq. (1). Fig. 1a shows the
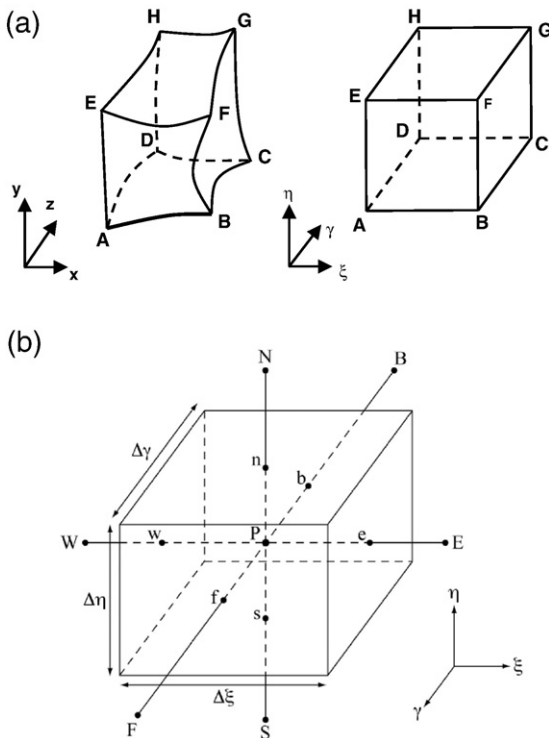
Table 1
Input data for case 1

Reservoir data	Initial conditions	Physical properties and well conditions
Reservoir dimension ($L_x=L_y=170.69$ m, $L_z=30.48$ m)	Water saturation $S_{wi}=0.17$	Water viscosity = 1×10^{-3} Pa s
	Reservoir pressure = 10.342 MPa (1500 psi)	Water injection rate = 9.2×10^{-4} m^3/s (500 barrels/d)
Absolute permeability ($K_{xx}=K_{yy}=K_{zz}$) = 1.0×10^{-14} m^2 (10 mD) Porosity = 0.350	Overall fraction of hydrocarbon components (C1, C3, C6, C10, C15, C20) = 0.5, 0.03, 0.07, 0.2, 0.15, 0.05 0.5, 0.03, 0.07, 0.2, 0.15, 0.05	Bottom hole pressure = 8.963 MPa (1300 psi)

physical and computational domains. Eq. (1) can be written in a boundary-fitted coordinate system using the following transformation:

$$\xi = \xi(x,y,z); \eta = \eta(x,y,z); \gamma = \gamma(x,y,z) \tag{6}$$

The transformed equation for the i-th component is given by

$$\frac{\partial}{\partial t}\left(\frac{\phi N_i}{J_t}\right) - \frac{\partial}{\partial \xi}\left(\sum_{j=1}^{np} D_{11ij}\frac{\partial \Phi_j}{\partial \xi}\right) - \frac{\partial}{\partial \xi}\left(\sum_{j=1}^{np} D_{12ij}\frac{\partial \Phi_j}{\partial \eta}\right) - \frac{\partial}{\partial \xi}\left(\sum_{j=1}^{np} D_{13ij}\frac{\partial \Phi_j}{\partial \gamma}\right)$$
$$- \frac{\partial}{\partial \eta}\left(\sum_{j=1}^{np} D_{21ij}\frac{\partial \Phi_j}{\partial \xi}\right) - \frac{\partial}{\partial \eta}\left(\sum_{j=1}^{np} D_{22ij}\frac{\partial \Phi_j}{\partial \eta}\right) - \frac{\partial}{\partial \eta}\left(\sum_{j=1}^{np} D_{23ij}\frac{\partial \Phi_j}{\partial \gamma}\right)$$
$$- \frac{\partial}{\partial \gamma}\left(\sum_{j=1}^{np} D_{31ij}\frac{\partial \Phi_j}{\partial \xi}\right) - \frac{\partial}{\partial \gamma}\left(\sum_{j=1}^{np} D_{32ij}\frac{\partial \Phi_j}{\partial \eta}\right) - \frac{\partial}{\partial \gamma}\left(\sum_{j=1}^{np} D_{33ij}\frac{\partial \Phi_j}{\partial \gamma}\right) - \frac{q_i}{V_b J_t} = 0 \tag{7}$$

where J_t is the Jacobian of the transformation and the tensor D involves fluid, reservoir, and geometric information. It is worthwhile
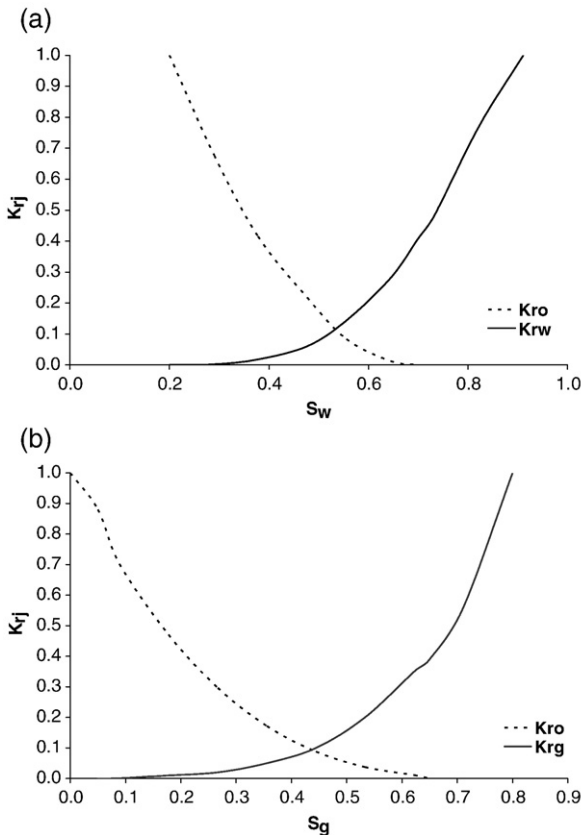

Fig. 3. Relative permeability curves (a) oil–water, (b) oil–gas.

to mention that both the D and K tensors are symmetric and the D tensor is always a full tensor with nine entries, while K is represented as a diagonal tensor in some cases. The entries of D are given by

$$D_{11ij} = \frac{\xi_j x_{ij}\lambda_j}{J_t}\left(\xi_x^2 K_{xx} + \xi_y^2 K_{yy} + \xi_z^2 K_{zz} + 2\xi_x\xi_y K_{xy} + 2\xi_x\xi_z K_{xz} + 2\xi_y\xi_z K_{yz}\right)$$

$$D_{12ij} = \frac{\xi_j x_{ij}\lambda_j}{J_t}\left(\begin{array}{c}\xi_x\eta_x K_{xx} + \xi_y\eta_y K_{yy} + \xi_z\eta_z K_{zz} + \left(\xi_x\eta_y + \xi_y\eta_x\right)K_{xy} + \\ \left(\xi_x\eta_z + \xi_z\eta_x\right)K_{xz} + \left(\xi_y\eta_z + \xi_z\eta_y\right)K_{xz}\end{array}\right)$$

$$D_{13ij} = \frac{\xi_j x_{ij}\lambda_j}{J_t}\left(\begin{array}{c}\xi_x\gamma_x K_{xx} + \xi_y\gamma_y K_{yy} + \xi_z\gamma_z K_{zz} + \left(\xi_x\gamma_y + \xi_y\gamma_x\right)K_{xy} + \\ \left(\xi_x\gamma_z + \xi_z\gamma_x\right)K_{xz} + \left(\xi_y\gamma_z + \xi_z\gamma_y\right)K_{yz}\end{array}\right) \tag{8}$$

$$D_{22ij} = \frac{\xi_j x_{ij}\lambda_j}{J_t}\left(\eta_x^2 K_{xx} + \eta_y^2 K_{yy} + \eta_z^2 K_{zz} + 2\eta_x\eta_y K_{xy} + 2\eta_x\eta_z K_{xz} + 2\eta_y\eta_z K_{yz}\right)$$

$$D_{23ij} = \frac{\xi_j x_{ij}\lambda_j}{J_t}\left(\begin{array}{c}\eta_x\gamma_x K_{xx} + \eta_y\gamma_y K_{yy} + \eta_z\gamma_z K_{zz} + \left(\eta_x\gamma_y + \eta_y\gamma_x\right)K_{xy} + \\ \left(\eta_x\gamma_z + \eta_z\gamma_x\right)K_{xz} + \left(\eta_y\gamma_z + \eta_z\gamma_y\right)K_{yz}\end{array}\right)$$

$$D_{33ij} = \frac{\xi_j x_{ij}\lambda_j}{J_t}\left(\gamma_x^2 K_{xx} + \gamma_y^2 K_{yy} + \gamma_z^2 K_{zz} + 2\gamma_x\gamma_y K_{xy} + 2\gamma_x\gamma_z K_{xz} + 2\gamma_y\gamma_z K_{yz}\right)$$

In Eq. (8) $\xi_x, \xi_y,..., \eta_x, \eta_y,...,\gamma_x, \gamma_y, ...$ are the direct metrics of the transformation, which are evaluated numerically.

Integrating Eq. (7) into the control volume of Fig. 1b and time results in the following approximate equation:

$$\left(\frac{\phi N_i}{J_t}\right)_P^{n+1}\frac{\Delta V}{\Delta t} - \left(\frac{\phi N_i}{J_t}\right)_P^{n}\frac{\Delta V}{\Delta t} - \sum_{j=1}^{np} D_{11ij,e}^{n+1}\left.\frac{\partial \Phi_j}{\partial \xi}\right|_e^{n+1}\Delta\eta\Delta\gamma$$
$$+ \sum_{j=1}^{np} D_{11ij,w}^{n+1}\left.\frac{\partial \Phi_j}{\partial \xi}\right|_w^{n+1}\Delta\eta\Delta\gamma - \sum_{j=1}^{np} D_{12ij,e}^{n+1}\left.\frac{\partial \Phi_j}{\partial \eta}\right|_e\Delta\eta\Delta\gamma$$
$$+ \sum_{j=1}^{np} D_{12ij,w}^{n+1}\left.\frac{\partial \Phi_j}{\partial \eta}\right|_w^{n}\Delta\eta\Delta\gamma - \sum_{j=1}^{np} D_{13ij,e}^{n+1}\left.\frac{\partial \Phi_j}{\partial \gamma}\right|_e\Delta\eta\Delta\gamma$$
$$+ \sum_{j=1}^{np} D_{13ij,w}^{n+1}\left.\frac{\partial \Phi_j}{\partial \gamma}\right|_w^{n}\Delta\eta\Delta\gamma - \sum_{j=1}^{np} D_{21ij,n}^{n+1}\left.\frac{\partial \Phi_j}{\partial \xi}\right|_n^{n}\Delta\xi\Delta\gamma$$
$$+ \sum_{j=1}^{np} D_{21ij,s}^{n+1}\left.\frac{\partial \Phi_j}{\partial \xi}\right|_s^{n}\Delta\xi\Delta\gamma - \sum_{j=1}^{np} D_{22ij,n}^{n+1}\left.\frac{\partial \Phi_j}{\partial \eta}\right|_n^{n+1}\Delta\xi\Delta\gamma$$
$$+ \sum_{j=1}^{np} D_{22ij,s}^{n+1}\left.\frac{\partial \Phi_j}{\partial \eta}\right|_s^{n+1}\Delta\xi\Delta\gamma - \sum_{j=1}^{np} D_{23ij,n}^{n+1}\left.\frac{\partial \Phi_j}{\partial \gamma}\right|_n^{n}\Delta\xi\Delta\gamma \tag{9}$$
$$+ \sum_{j=1}^{np} D_{23ij,s}^{n+1}\left.\frac{\partial \Phi_j}{\partial \gamma}\right|_s^{n}\Delta\xi\Delta\gamma - \sum_{j=1}^{np} D_{31ij,f}^{n+1}\left.\frac{\partial \Phi_j}{\partial \xi}\right|_f^{n}\Delta\xi\Delta\eta$$
$$+ \sum_{j=1}^{np} D_{31ij,b}^{n+1}\left.\frac{\partial \Phi_j}{\partial \xi}\right|_b^{n}\Delta\xi\Delta\eta - \sum_{j=1}^{np} D_{32ij,f}^{n+1}\left.\frac{\partial \Phi_j}{\partial \eta}\right|_f^{n}\Delta\xi\Delta\eta$$
$$+ \sum_{j=1}^{np} D_{32ij,b}^{n+1}\left.\frac{\partial \Phi_j}{\partial \eta}\right|_b^{n}\Delta\xi\Delta\eta - \sum_{j=1}^{np} D_{33ij,f}^{n+1}\left.\frac{\partial \Phi_j}{\partial \gamma}\right|_f^{n+1}\Delta\xi\Delta\eta$$
$$+ \sum_{j=1}^{np} D_{33ij,b}^{n+1}\left.\frac{\partial \Phi_j}{\partial \gamma}\right|_b^{n+1}\Delta\xi\Delta\eta - \frac{q_{i,P}^{n+1}\Delta V}{V_b J_{t,P}} = 0$$

All the derivatives in Eq. (9) are evaluated using the central difference scheme, and the fluid and phase properties that are grouped into the D tensor are evaluated by the upstream difference
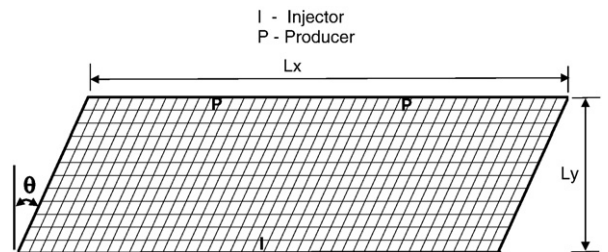

Fig. 4. Top view of reservoir used for case 2.

Table 2
Input data for case 2

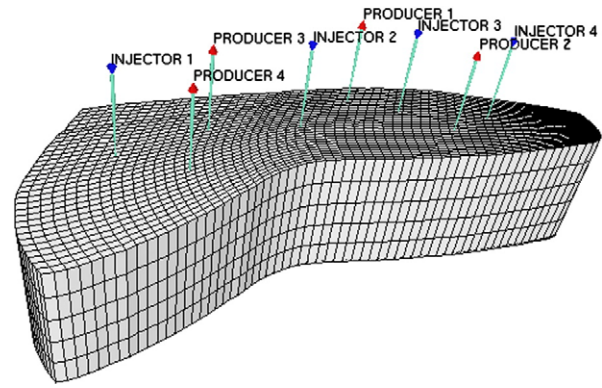| Reservoir data	Initial conditions	Physical properties and well conditions
Reservoir dimension ($L_x = 1737.36$ m, $L_y = 548.64$ m, $L_z = 18.29$ m)	Water saturation $S_{wi} = 0.17$	Water viscosity = 1×10^{-3} Pa s
	Reservoir pressure = 10.342 MPa (1500 psi)	Water injection rate = 4.6×10^{-3} m³/s (2500 barrels/d)
Absolute permeability	Overall fraction of hydrocarbon components (C1, C3, C6, C10, C15, C20) = 0.5, 0.03, 0.07, 0.2, 0.15, 0.05	Bottom hole pressure = 7.584 MPa (1100 psi)
($K_{xx} = K_{yy} = K_{zz}) = 1.0 \times 10^{-13}$ m² (100 mD) − isotropic $K_{xx} = 1.0 \times 10^{-13}$ m² (100 mD), $K_{yy} = 5.0 \times 10^{-13}$ m² (500 mD), $K_{zz} = 1.0 \times 10^{-14}$ m² (10 mD) − anisotropic Porosity = 0.350		

Fig. 5. A 60×32×5 mesh configuration for case 3.

which will be referred as case 1, is the simulation of water flooding in a quarter-of-five spot and the simultaneous flow of water, oil, and gas. We have chosen this case because we can verify the results using
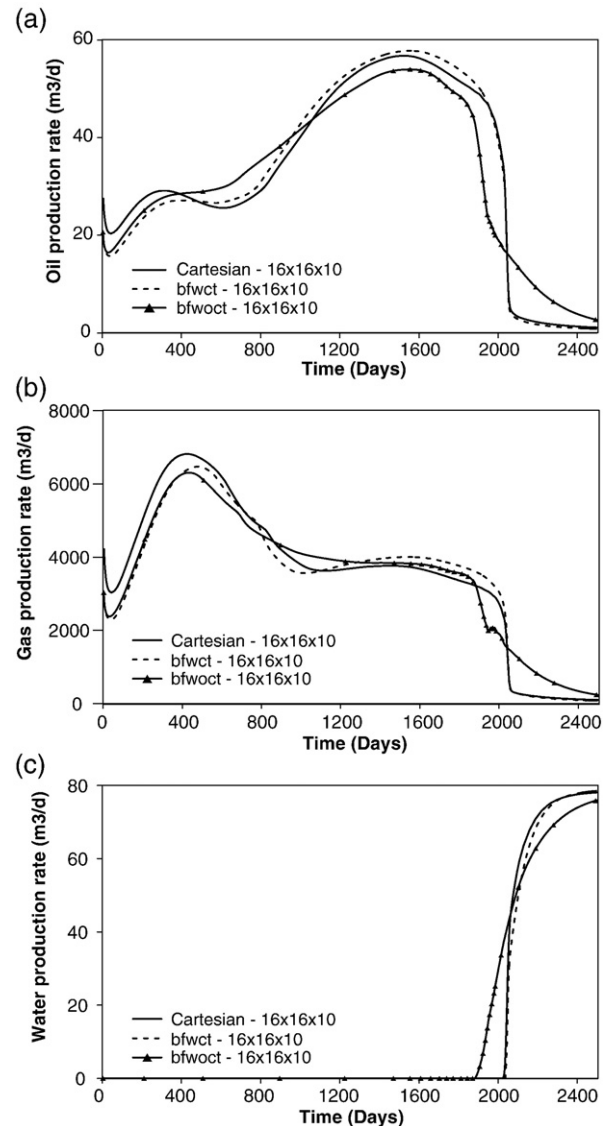
scheme. Considering, for instance, the interface *e* of Fig. 1b, the mobility of the fluid phase *j* is evaluated by the upstream scheme as

$$
\lambda_{j,e} = \begin{cases} \lambda_{j,P} \; if \; D_{11ij}\dfrac{\partial \Phi_j}{\partial \xi} + D_{12ij}\dfrac{\partial \Phi_j}{\partial \eta} + D_{12ij}\dfrac{\partial \Phi_j}{\partial \gamma}\bigg|_e < 0 \\[2mm] \lambda_{j,E} \; if \; D_{11ij}\dfrac{\partial \Phi_j}{\partial \xi} + D_{12ij}\dfrac{\partial \Phi_j}{\partial \eta} + D_{12ij}\dfrac{\partial \Phi_j}{\partial \gamma}\bigg|_e > 0 \end{cases}
\tag{10}
$$

The same approach is used to evaluate other fluid proprieties at each interface of the control volume.

Next, the Newton method is used to linearize the equations. In order to not increase the number of non-zero diagonals in the coefficient matrix of the linear system of equations, the cross derivatives were included in the right-hand side of the residual function, resulting in a semi-implicit procedure. This procedure can reduce the convergence rate of the linear system if the mesh is highly distorted. However, this procedure reproduces the exact mass flow rate along each interface of the control volume. Finally, it is important to mention that this procedure results in a seven diagonal matrix similar to the corner-point procedures used in most commercial codes, but in this procedure all mass fluxes are correctly evaluated, no matter how distorted the mesh is.

4. Test problems

In order to investigate the effect of cross derivatives in the numerical results, we performed three case studies. The first case,

Table 3
Input data for case 3

Data of the reservoir	Initial conditions	Physical properties and well conditions
Absolute permeability ($K_{xx} = 1.0 \times 10^{-13}$ m² (100 mD), $K_{yy} = 5.0 \times 10^{-13}$ m² (500 mD), $K_{zz} = 1.0 \times 10^{-14}$ m² (10 mD)	Water saturation $S_{wi} = 0.17$	Water viscosity = 1×10^{-3} Pa s
	Reservoir pressure = 10.342 MPa (1500 psi)	Total water injection rate = 1.1×10^{-2} m³/s (6000 barrels/d)
Thickness = 15.24 m	Overall fraction of hydrocarbon components (C10, C15, C20) = 0.7, 0.2, 0.1	Bottom hole pressure = 10.342 MPa (1500 psi)
Area = 3.4706×10^4 m² Porosity = 0.350		

Fig. 6. Results for case 1 (a) oil production rate vs. time (b) gas production rate vs. time (c) water production rate vs. time.

boundary-fitted coordinates with the ones using the original Cartesian meshes from GPAS that have been tested and validated with commercial codes and in-house simulators called UTCHEM (Delshad et al., 1996) and UTCOMP (Chang et al., 1990) developed in the Center for Petroleum and Geosystems Engineering at the University of Texas at Austin. This problem was solved using a uniform Cartesian mesh (16×16×10 using the original code) and a corner-point mesh (16×16×10 using the modified code) as shown in Fig. 2. The fluid and reservoir properties are given in Table 1. The relative perme-abilities are evaluated using the Stone II Model (Stone, 1973). The curves used to evaluate these relative permeabilities are presented in Fig. 3. Since the results should be independent of the mesh used, it is expected that we will obtain close agreement between the non-orthogonal and Cartesian meshes if the fluxes and geometric information are computed correctly.

The second case is a distorted rectangular domain. This case was used by Hegre et al. (1986) using the finite element approach and Aavatsmark et al. (1998) using corner-point meshes. Fig. 4 presents the top view of the reservoir. All of the wells are completely perforated along the reservoir thickness. The angle of the distortion of the mesh was changed from 5 to 25°. In order to verify the effect of entries of the absolute tensor for each angle, two simulations were performed: one
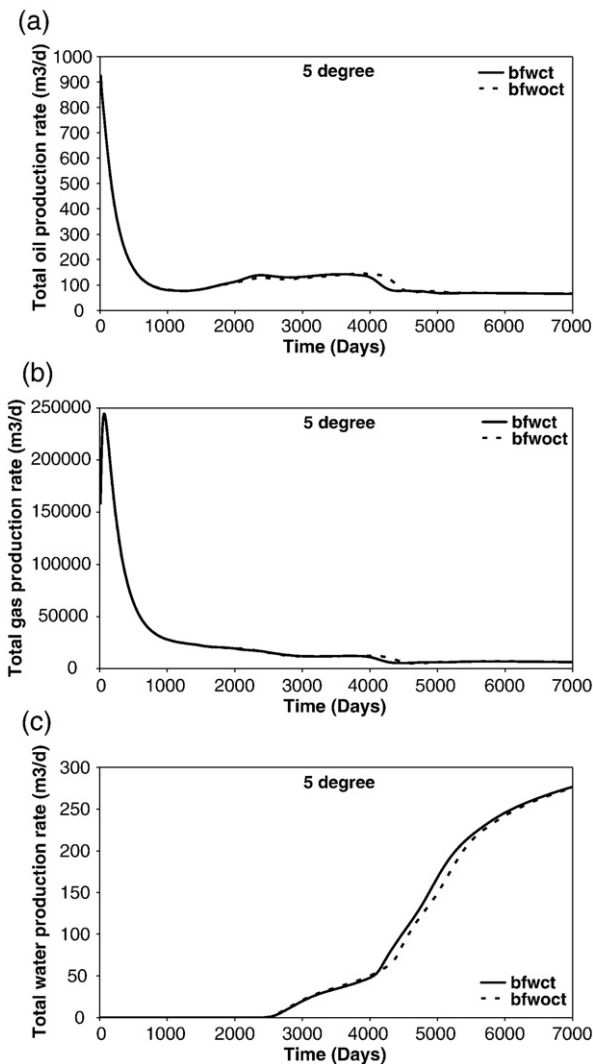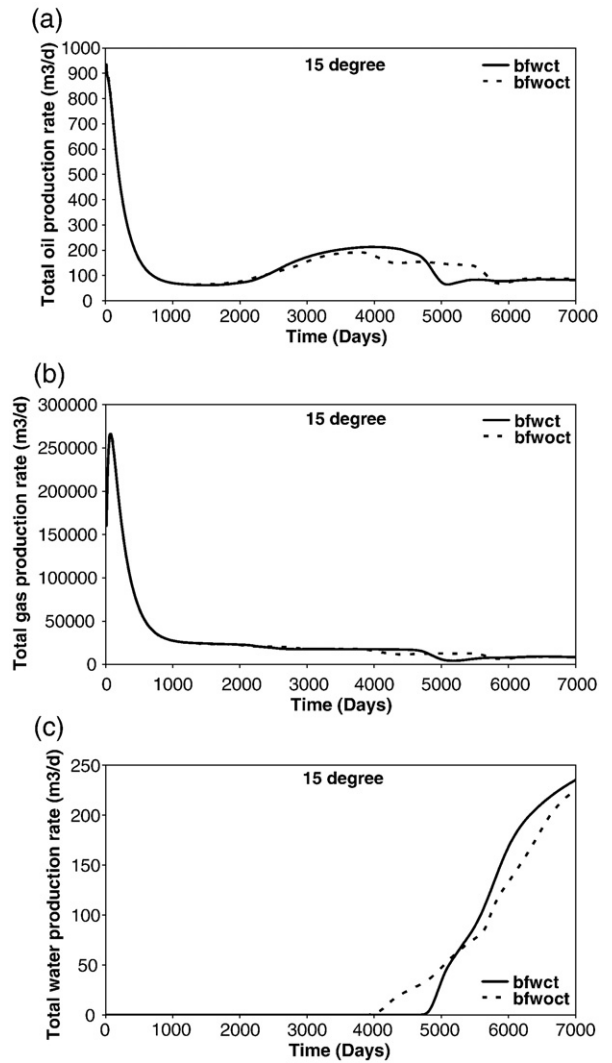
Fig. 8. Results for case 2: isotropic reservoir, 15 °(a) oil production rate vs. time (b) gas production rate vs. time (c) water production rate vs. time.

for an isotropic reservoir and another for a diagonal anisotropic reservoir. This is a water flooding case with the simultaneous flow of water, gas, and oil. The same set of relative permeability curves as case 1 was used for this study. The fluid and reservoir conditions are given in Table 2.

The last case is a domain that mimics the boundaries of a real reservoir. Although the angle of distortion varies along the reservoir, the variation of distortion is not large. This is a water flooding case, and only oil and water exist in the reservoir. The fluid and reservoir properties are given in Table 3. In this case we used the relative permeability curves given in Fig. 3a. Fig. 5 presents a 60×3×5 mesh employed to simulate this case.

5. Results

Fig. 6 presents the results in terms of volumetric rate at standard conditions for oil, gas, and water phases for case 1. In the following figures, bfwct and bfwoct stand for boundary fitted with and without cross terms, respectively. Although the non-orthogonal mesh pre-sented in Fig. 2 is highly distorted and unequally spaced, the results, considering the discretized equations with cross derivatives included, are very close to the ones obtained with a regular equally spaced Cartesian mesh. On the other hand, the results, when the cross

Fig. 7. Results for case 2: isotropic reservoir, 5° (a) oil production rate vs. time (b) gas production rate vs. time (c) water production rate vs. time.

derivatives were neglected are not in agreement when compared to the results obtained with the Cartesian mesh.

Figs. 7–9 show the results for cumulative oil, gas, and water volumetric rates for case 2, considering an isotropic reservoir with varying angles of grid distortion changing from 5 to 25°. For 5°, there are only small differences between the results with and without cross terms, suggesting that cross derivatives can in fact be neglected. However, when the angle of distortion is increased to 15°, large differences appear in the results (as can be seen in Fig. 8), especially for oil and water volumetric rates. Although the results for angles larger than 25° are not presented, large differences were observed in the results for cases with and without cross derivatives included in the discretization. Despite the large differences observed for oil and water rates, the curves obtained for gas except near the water breakthrough are very similar. Such behavior can be explained based on the product of molar densities, molar fraction and relative mobilities of the phases. The cross derivatives are used in evaluation of mass flow rate, and all cross derivatives are multiplied by the product of physical properties of each phase. For this water flooding and the initial amount of gas in the reservoir, the product mentioned before for the gas phase is smaller than for water and oil phases. It is important to note that the mass flow rate at each interface of the control volume is the sum of

Fig. 10. Results for case 2: anisotropic reservoir, 5° (a) oil production rate vs. time (b) gas production rate vs. time (c) water production rate vs. time.
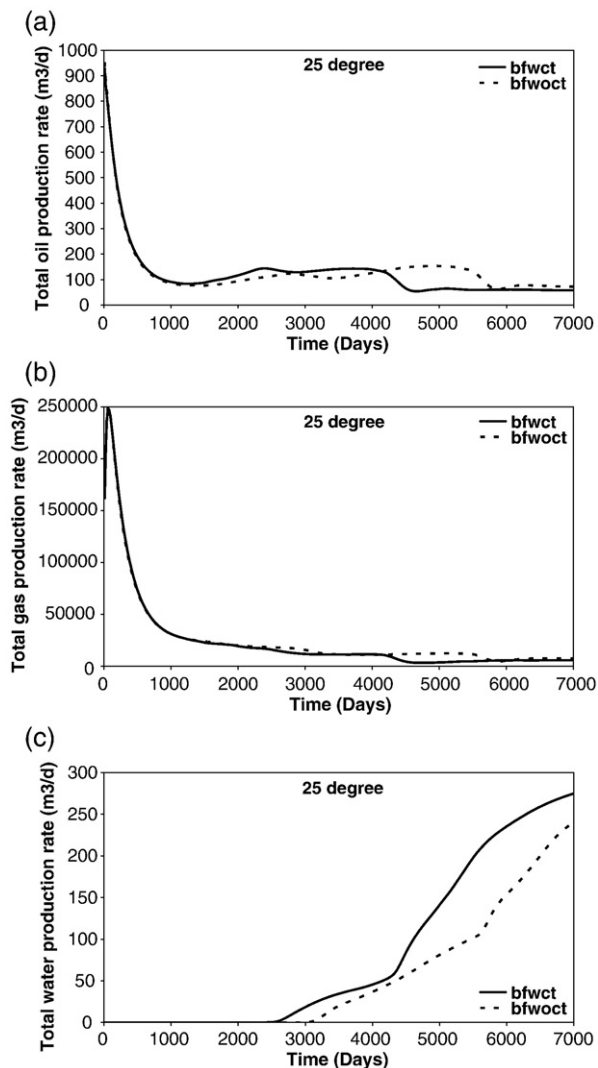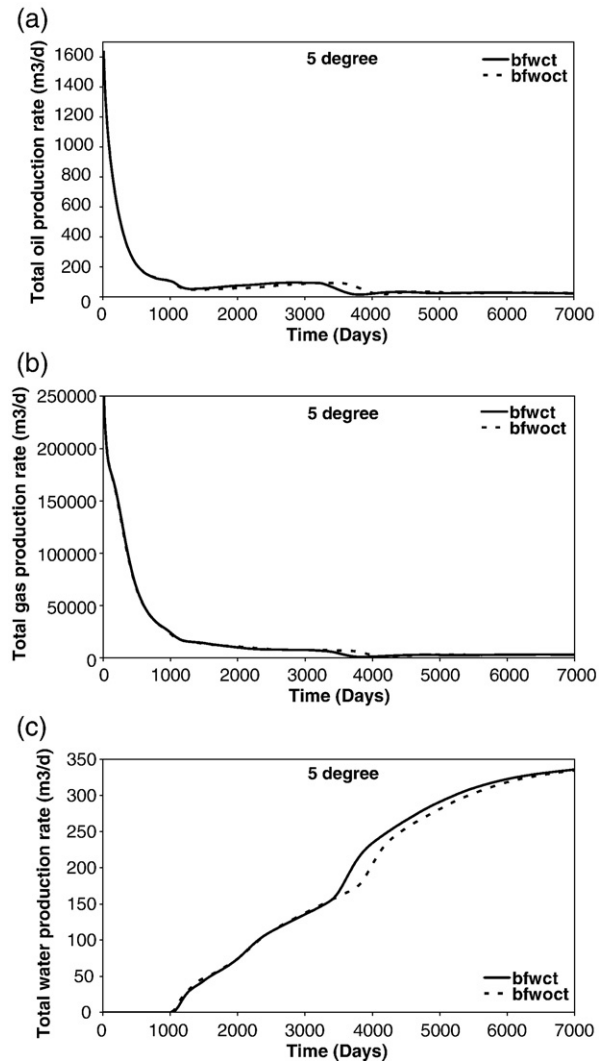
Fig. 9. Results for case 2: isotropic reservoir, 25° (a) oil production rate vs. time (b) gas production rate vs. time (c) water production rate vs. time.

direct and cross derivatives multiplied by fluid proprieties. If the value of fluid proprieties is smaller for one phase, then the effect of the cross derivatives will be smaller. Because the gas has the smallest product, we can expect its influence on the cross derivatives to be the smallest. It is also observed that the differences in the results for water are higher than those for oil, and the explanation again is based on the product of the physical properties evaluated at the control volume interface.

Figs. 10–12 present the results for case 2 with anisotropic permeabilities and angles changing from 5 to 25°. From these figures, it is possible to infer that the cross derivatives play an important role, since the differences in the results are now amplified when compared to the same angle for the isotropic case. Although the results for angles larger than 25° are not presented, the differences in the results were larger than those observed for the isotropic case using the same angle.

Fig. 13 presents the results for case 3. Comparison of the results for the case using cross derivatives with 45×24×4 and 60×32×5 meshes shows close agreement. The same behavior is observed with the case without cross derivatives. On the other hand, comparison of the results using formulas with and without cross derivatives displays different results. Once again, the following is the reason for such

behavior. When cross derivatives are neglected, convergence is not achieved. This is because the approximate equations do not produce the original set of partial differential equations when the mesh is refined, since some parts of the mass flow rate are neglected. More importantly, the difference in simulation results with and without cross derivatives does not decrease when the mesh is refined. It is important to mention that both procedures, with and without cross derivatives, are mass conservative in nature, since we are employing the finite-volume approach. However, the approximate set of equations without cross derivates will produce a set of partial differential equations that is different from the original one, when the mesh is refined as was shown in the results presented in this section.

6. Conclusions

This work presented an investigation of the effect of cross derivatives in a fully implicit compositional simulator called GPAS. The tests were done for several reservoirs with different geometries and for simultaneous flows of water, gas, and oil with several hydrocarbon components. Isotropic and anisotropic reservoirs were also investigated. From the results of the simulation studies carried out, it is possible to infer that neglecting the cross derivatives in the
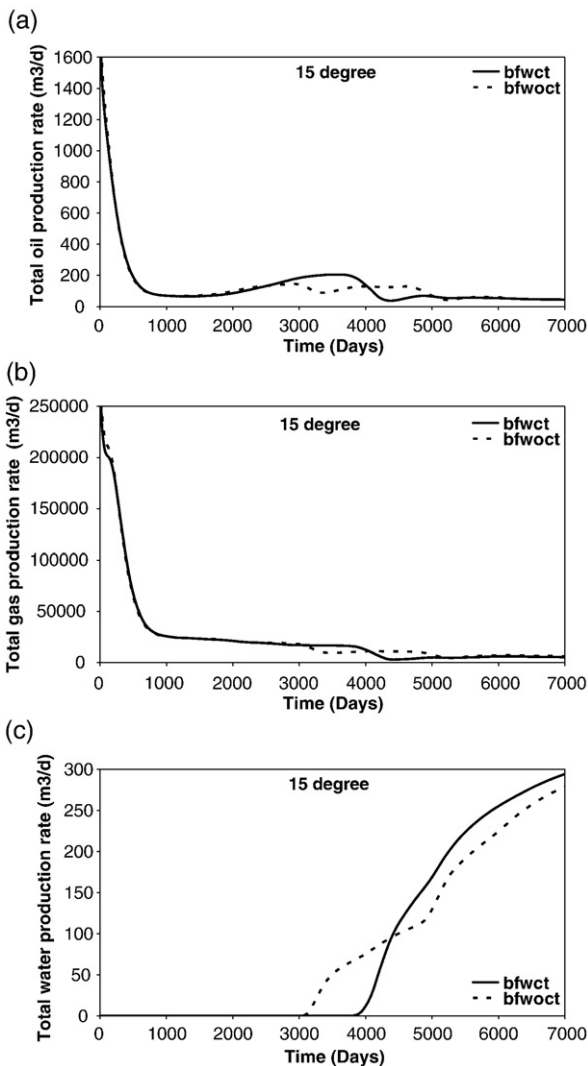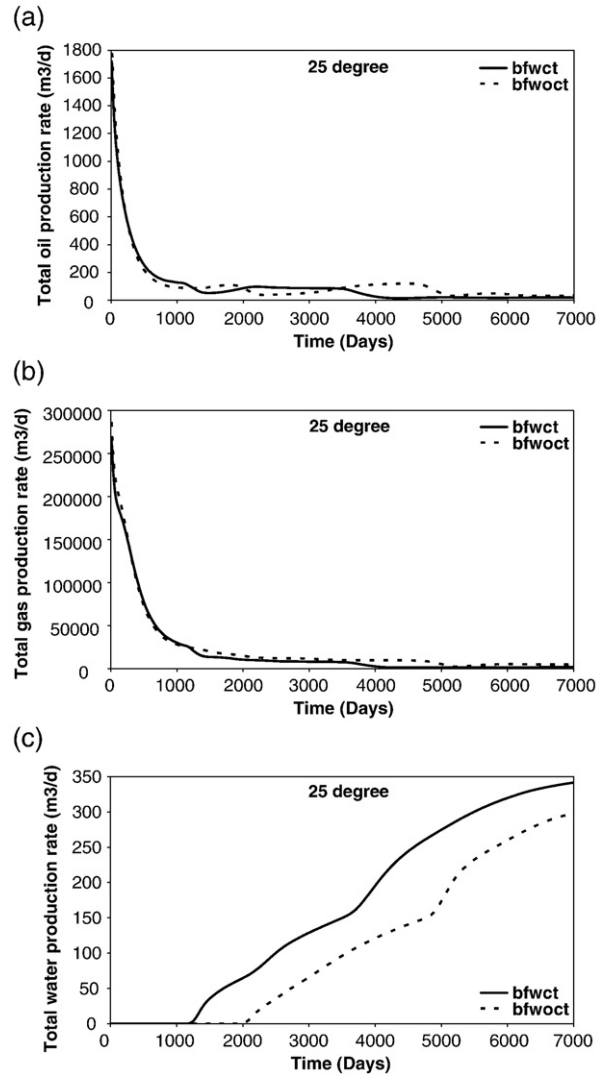
Fig. 12. Results for case 2: anisotropic reservoir, 25° (a) oil production rate vs. time (b) gas production rate vs. time (c) water production rate vs. time.

discretized equations produces inaccuracies in the results even when the mesh is distorted by a small amount. Also, the differences in the simulation results do not decrease when the mesh is refined. The main reason for such behavior is easily explained. When the cross derivatives are neglected, some parts of the equations that must be included in the computations of mass flow rate are neglected. If the mesh is orthogonal, the neglected mass flow rate is in fact zero. However, when the mesh is distorted, the neglected terms are not zero and should be taken into account in the mass flow evaluation. In conclusion, simulators that employ boundary-fitted coordinates to mimic important features of the reservoir should include cross derivatives, otherwise serious errors will be introduced into the numerical simulations.

Fig. 11. Results for case 2: anisotropic reservoir, 15° (a) oil production rate vs. time (b) gas production rate vs. time (c) water production rate vs. time.
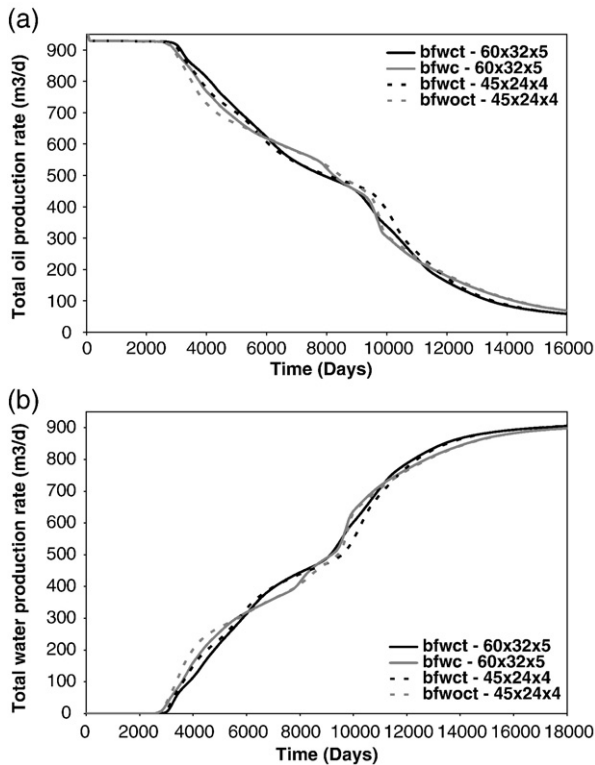
Fig. 13. Results for case 3 (a) oil production rate (b) water production rate vs. time.

References

Aavatsmark, I., Barkve, T., Mannseth, T., 1998. Control-volume discretization methods for 3D quadrilateral grids in inhomogeneous, anisotropic reservoirs. SPE Journal 3 (2), 146–154.

Aziz, K., 1993. Reservoir simulation grids: opportunities and problems. Journal Petroleum Technology 45 (7), 658–663.

Chang, Y., Pope, G., Sepehrnoori, K., 1990. A higher-order finite-difference compositional simulator. Journal of Petroleum Science and Engineering 5 (1), 35–50.

Delshad, M., Pope, G., Sepehrnoori, K., 1996. A compositional simulator for modeling sufactant enhanced aquifer remediation, 1 formulation. Journal of Contaminant Hydrology 23 (4), 303–327.

Edwards, M.G., 1998a. Cross flow tensors and finite volume approximation with deferred correction. Computer Methods in Applied Mechanics and Engineering 51, 143–161.

Edwards, M.G., 1998b. Simulation with a full tensor coefficient velocity field recovered from a diagonal tensor solution, SPE 49073. SPE Annual Technical Conference and Exhibition, New Orleans, USA.

Edwards, M.G., Rogers, C.F., 1998. Finite volume discretization with imposed flux continuity for general tensor pressure equation. Computational Sciences 2, 259–290.

Gropp, W., Lusk, E., Skjellum, A., 1999. Using MPI: Portable Parallel Programming with the Message-Passing Interface,, Second Edition. The MIT Press, Massachusetts.

Hegre, T.M., Dalen, V., Henriquez, A., 1986. Generalized transmissibilities for distorted grids in reservoir simulation, SPE 15622. 61st Annual Technical Conference of Society of Petroleum Engineers, New Orleans, USA.

Hirasaki, G.J., O'Dell, P.M., 1970. Representation of reservoir geometry for numerical simulation. SPE Journal (December) 393–404.

Leventhal, S.H., Klein, M.H., Culham, W.E., 1985. Curvilinear coordinate systems for reservoir simulation. SPEJ 893–904.

Maliska, C.R., 2004. Heat Transfer and Computational Fluid Mechanics, Second Edition. LTC, Rio de Janeiro, Brazil. (In Portuguese).

Maliska, C.R., da Silva, A.F.C., Czesnat, A.O., Lucianetti, R.M., Maliska Jr., C.R., 1997. Three-dimensional multiphase flow simulation in petroleum reservoirs using the mass fractions as dependent variables, SPE 39067-MS. Latin American and Caribbean Petroleum Engineering Conference, Rio de Janeiro, Brazil.

Marcondes, F., Cordazzo, J., Cemin, A., Beviláqua, A.L.S., Silva, A.F.C., Maliska, C.R., 2005a. Analysis of several software used in petroleum reservoir simulation. 18th International Congress of Mechanical Engineering, November 6-11, Ouro Preto, MG, Brazil.

Marcondes, F., Han, C., Sepehrnoori, K., 2005b. Implementation of corner point mesh into a parallel, fully implicit, equation of state compositional reservoir simulator. 18th International Congress of Mechanical Engineering, November 6-11, Ouro Preto, MG, Brazil.

Parashar, M., Wheeler, J.A., Pope, G., Wang, K., Wang, P., 1997. A new generation EOS compositional reservoir simulator: Part II — framework and multiprocessing, SPE 37977. SPE Reservoir Simulation Symposium, Dallas, USA.

Prévost, M., Edwards, M.G., 2002. Streamline tracing on curvilinear structured and unstructured grids. SPEJ 139–148.

Sheldon, J.W., Dougherty, E.D., 1961. The approximation of secondary recovery projects using moving interfaces, SPE 182. 36th Annual Fall Meeting, Dallas, USA.

Stone, H.L., 1973. Estimation of three-phase relative permeability and residual data. Journal of Canadian Petroleum Technology 12 (4), 53–61.

Wadsley, W.A., 1980. Modelling reservoir geometry with non-rectangular coordinates grids, SPE 9369. 55th Annual Fall Technical Conference and Exhibition of Society of Petroleum Engineers of AIME, Dallas, USA.

Wang, P., Yotov, I., Wheeler, M., Arbogast, T., Dawson, C., Parashar, M., Sepehrnoori, K., 1997. A new generation EOS compositional reservoir simulator: Part I — formulation and discretization, SPE 37079. SPE Reservoir Simulation Symposium, Dallas, USA.